Viscoplastic friction and microstructural evolution behavior of laser-clad Co−Cr−Ni−Mo coating

Rui-di LI[1,2], Jing-long LI[1,2], Yi LIANG[1,2], Cheng-zhong JI[1,2], Tie-chui YUAN[3]

1. State Key Laboratory of Solidification Processing, Northwestern Polytechnical University, Xi'an 710072, China;
2. Shaanxi Key Laboratory of Friction Welding Technologies,
Northwestern Polytechnical University, Xi'an 710072, China;
3. State Key Laboratory of Powder Metallurgy, Central South University, Changsha 410083, China

Abstract: The viscoplastic friction and nanostructure formation mechanism of laser-clad Co-based coating were studied by rotary friction between laser-clad Co−Cr−Ni−Mo coating and WC−Co rod. The friction coefficient, friction interface temperature and axial displacement—time curves during rotary friction process were measured. The results showed that all the curves firstly experienced rising stage and then steady stage. The rising stage corresponded to sliding friction while the steady stage corresponded to viscoplastic friction. After viscoplastic friction processing, three typical zones of viscoplastic deformation zone, thermo-mechanically affected zone, and original laser-clad zone can be observed successively from the friction surface to the interior. The viscoplastic deformation significantly crushed the network $M_{23}C_7$ phase in original laser-clad zone and made it dispersively distributed with equiaxial shape and in nano-scale. The viscoplastic zone, in width of 37−131 μm, is mainly characterized by refined $M_{23}C_7$ and α-Co phase with grain size bellow 50 nm, and even a small quantity of amorphous. Thus, the hardness of viscoplastic zone about HV997 was improved compared with the hardness of original laser-clad zone about HV600.
Key words: viscoplastic deformation; severe plastic deformation; laser cladding; Co−Cr−Ni−Mo coating; nanostructure; rotary friction

1 Introduction

Laser cladding is an effective alternative to improve the wear resistance and hardness of metallic materials owing to its special metallurgy behavior of laser radiation, high energy input, and accordingly rapid melting/solidification, which makes the reliable connection between the coating and substrate [1]. Therefore, investigation into the friction behavior of laser coating is a vital issue. Based on this, WANG et al [2] studied the abrasive wear behavior of laser-clad tool steel coatings. YAN et al [3,4] studied the tribology behavior of laser-clad Ni based and Co based coatings on substrates. GU et al [5−7] investigated the wear performance of pure Ti, TiC/Ti composites and TiN−Ti_5Si_3 composites by selective laser melting. However, the previous studies about laser-clad coating friction were limited to conventional rubbing, wear or

adhesive friction, during which the severe plastic flow and rapid temperature rising at the friction interface did not exist.

Viscoplastic friction, as a novel kind of friction, was detected and concerned in friction welding, during which the friction interface experiences friction heat generation, rapid temperature rising, plastic flow and dynamic recrystallization [8,9]. However, there were no literatures issuing the viscoplastic friction of laser cladding coating, since the laser cladding coating may service at viscoplastic condition. Thereby, the study on the viscoplastic friction behavior of laser-clad coating, including friction coefficient, friction interface temperature and abrasion loss, is considered to be necessary.

Additionally, owing to the intrinsic nature of severe plastic, the viscoplastic friction can be regarded as a severe plastic deformation (SPD) process, which can diminish the grain size of various metal materials and is

similar with equal-channel angular pressing (ECAP) [10], accumulative roll bonding (ARB) [11] and friction stir processing (FSP) [12,13]. Thereby, the viscoplastic friction may also modify the laser-clad microstructure and metallurgical defects [14] by high plastic deformation, inducing fine grain and accordingly excellent mechanical strength. However, the microstructure evolution of laser coating under the action of viscoplastic friction was still unknown, since it involves high gradient temperature, stress−strain, and accordingly complex grain crushing and dynamic recrystallization.

In the present work, the viscoplastic friction behavior between laser-clad Co−Cr−Ni−Mo and WC−Co cemented carbide was studied by rotary friction. The friction coefficient, interface temperature and abrasion loss during rotary friction were systematically measured by mechanics sensor system, infrared thermal imaging, high speed photography technology, respectively. In addition, the resultant microstructural evolution of laser coating under the action of plastic friction was investigated.

2 Experimental

In laser cladding experiments, the CO_2 laser had a maximum output power of 5 kW and it was equipped with a digital controlled multiaxis positioning and worktable. The substrate was A3 steel with the dimension of 50 mm×70 mm×10 mm. Before cladding, the substrate was surface polished to remove surface oxide. The material adopted was Co-based alloy powder with a nominal composition (mass fraction) of 0.5%−0.6% C, 24%−27% Cr, 8%−9% Ni, 3%−4% Mo, 3%−4% W, 1.6%−2% Si, 2%−3% Fe and Co in balance. The laser-clad parameters were as follows: laser power 2.0−3.5 kW, spot diameter 4 mm, scan speed 2−16 mm/s, powder feeding rate 15−50 mg/mm, and powder layer 0.2−1 mm.

After laser cladding experiments, the laser-clad substrates were cut into small friction samples with the dimensions of 20 mm×20 mm×10 mm. The friction tool was WC−Co rod with the diameter of 12 mm. Figure 1 shows the schematic of rotary friction experiment between WC−Co rod and laser-clad Co−Cr−Ni−Mo coating. Before the rotary friction, the WC−Co rod was rotated around its axis while the titanium rod was fixed. When the rotary speed reached the pre-set value, the laser-clad coating moved along the axis until contacted the carbide rod by hydraulic pressure, then the rotary friction process began. After the friction, the laser coating lost contact with carbide rod. The friction welding parameters were as follows: rotation speed 600−1500 r/min, axial pressure 5−10 kN. Moreover,

during the rotary friction process, the friction image was collected by a high-speed camera (Vision Research Inc., Phantom v 310) with a frame rate of 500 fps. The friction interface temperature was detected by an infrared thermal imaging system (InfraTec, VarioCAM®hr head-HS) with the frame rate of 60 fps. The torque and normal pressure were measured by a mechanical quantity sensor with frequency of 1000 Hz.
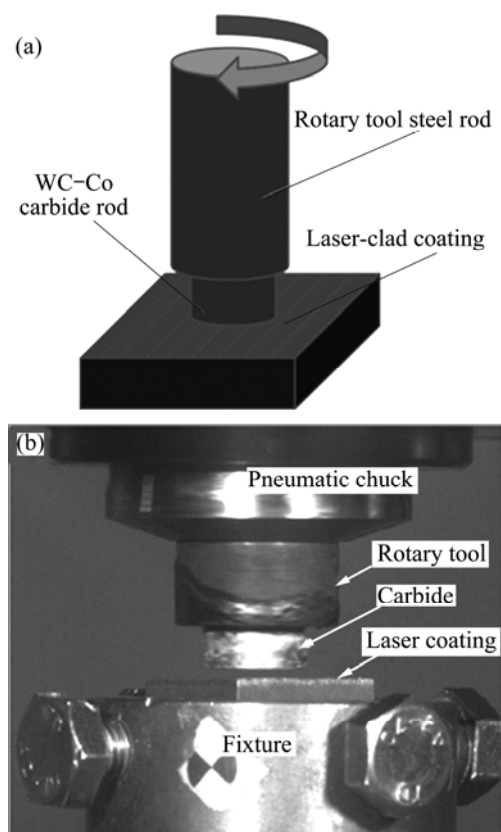

Fig. 1 Rotary friction apparatus between WC−Co carbide and laser-clad coating: (a) Diagrammatic drawing; (b) Actual tooling diagram

At last, the friction surface morphologies of laser coatings were characterized by a scanning electron microscope (SEM). Then the friction samples of laser coatings for metallographic examination were cut perpendicular to the friction surface and the samples for metallographic analysis were produced by standard methods. The microstructure was analyzed by SEM and the chemical composition was obtained by an energy dispersive X-ray (EDX) spectrometer. The micro-structure of viscoplastic deformation zone was measured by integration of focused ion beam (FIB) and transmission electron microscopy (TEM), and high-resolution transmission electron microscopy (HRTEM) with selected area electron diffraction (SAED) pattern. A microhardness measurement was carried out using a micro-Vickers hardness tester with an applied load of 3 N for 10 s.

3 Results and discussion

3.1 Viscoplastic friction behavior

3.1.1 Friction coefficient

The friction coefficients between laser-clad coating and cemented carbide under different rotary speeds are depicted in Fig. 2(a). The axial pressure of 7.5 kN was fixed as constant. It shows that the friction experienced two stages. Firstly, the friction coefficient rapidly increased to about 0.15. Then, the friction coefficient reduced slightly and went into a steady stage. In addition,

it can be found that the high rotary speed could lead to a more rapid rising rate of friction coefficient. Figure 2(b) shows the friction coefficient between laser coating and cemented carbide under different axial pressures. The rotary speed of 1500 r/min was fixed as constant. Similarly, friction coefficient variations also had the increasing stage and steady stage. Moreover, the high axial pressure could enable the rapid rising rate of friction coefficient.

3.1.2 Friction interface temperature

Figure 3 depicts the temperature images at different rotary time collected by infrared thermal imaging
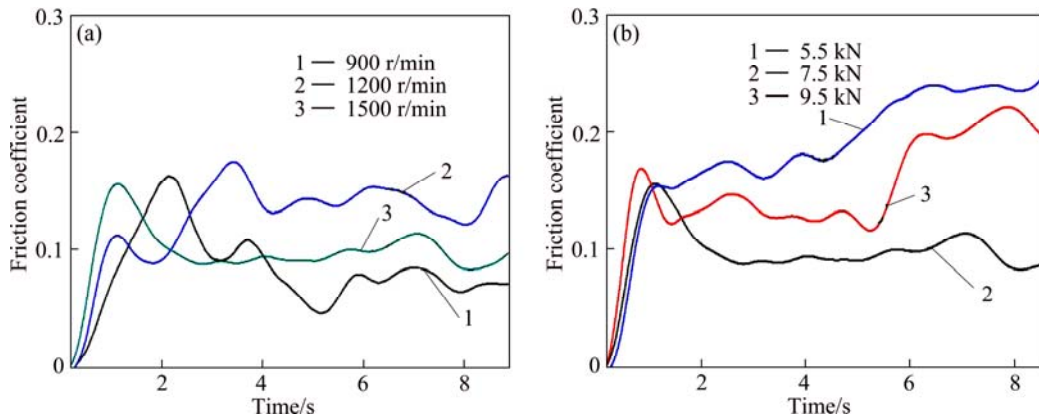

Fig. 2 Friction coefficient—time curves: (a) Under different rotary speeds with constant axial pressure of 7.5 kN; (b) Under different axial pressures with constant rotary speed of 1500 r/min
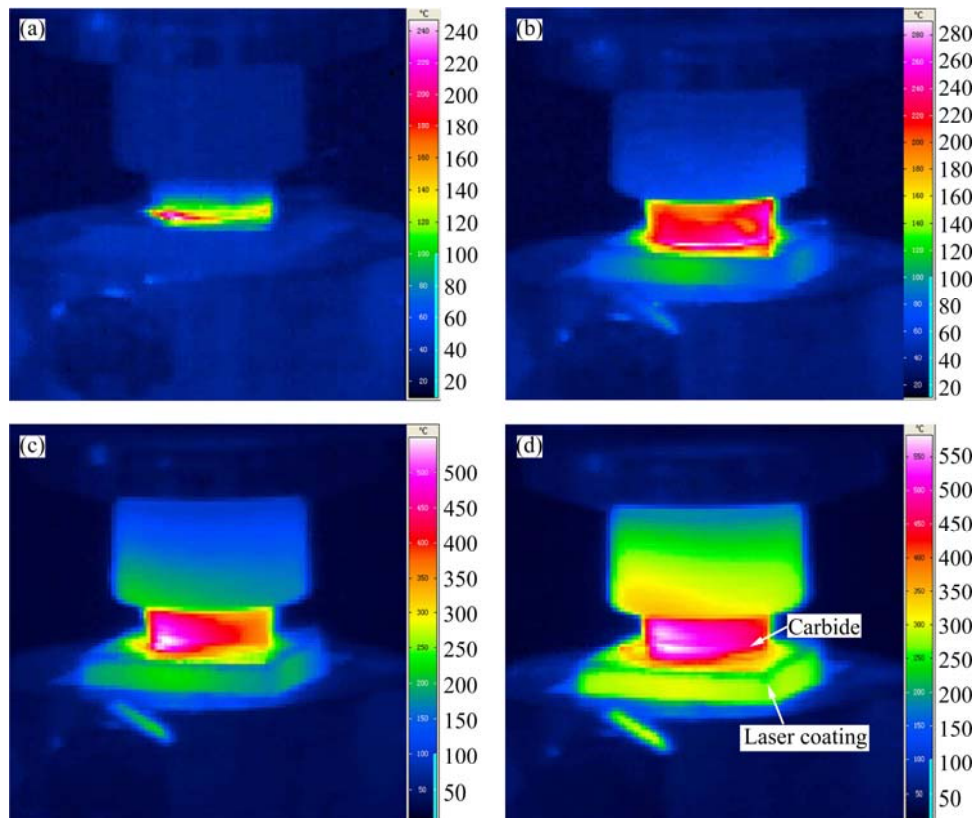

Fig. 3 Infrared thermal images showing temperature variation at different friction time: (a) 500 ms; (b) 2500 ms; (c) 6700 ms; (d) 10000 ms

technology. With the increase of friction time, the temperature of carbide and laser coating all increased obviously. In order to disclose the temperature evolution, the average temperature at friction interface was recorded. Figure 4(a) illustrates the relationship between friction interface temperature and time at different rotary speeds with the axial pressure of 7.5 kN. Similar to the friction coefficient—time curve, no matter what rotary speed was applied, the temperature firstly experienced a rapid rising stage and then entered a steady stage. At relatively low rotary speeds (600−1200 r/min), the temperatures of steady stage were about 350 °C, showing no obvious differences. When the rotary speed was increased to 1500 r/min, the temperature elevated to about 500 °C immediately. Meanwhile, with the increase of rotary speed, the temperature rising rate increased apparently. Figure 4(b) shows the relationship between the friction interface temperature and time under different axial pressures. The rotary speed of 1500 r/min was fixed as constant. At relatively low axial pressures of 5.5 and 7.5 kN, the temperature—time curves firstly

rose then reached a steady state, which were similar to the variation trends at different rotary speeds. However, at a high axial pressure of 9.5 kN, the temperature—time curve kept rising continuously. In addition, high axial pressure can also yield a more rapid rising rate of temperature.

3.1.3 Axial displacement and abrasion loss

Figure 5 illustrates the axial displacement—time curves, which were collected by high-speed photography technology. In all, no matter what friction parameters were applied, the axial displacement increased rapidly at the first stage and then reached a plateau. In more detail, the rotary speed and axial displacement all have remarkable effects on the axial displacement. When a more rapid rotary speed or higher axial pressure was applied, the as-received plateau value of axial displacement was higher. Moreover, the relatively high rotary speed and high axial pressure all could enable the rapid increasing rate, corresponding to the high curve slope. Figure 6 shows the relationship between abrasion loss and rotary speed and axial pressure. It should be
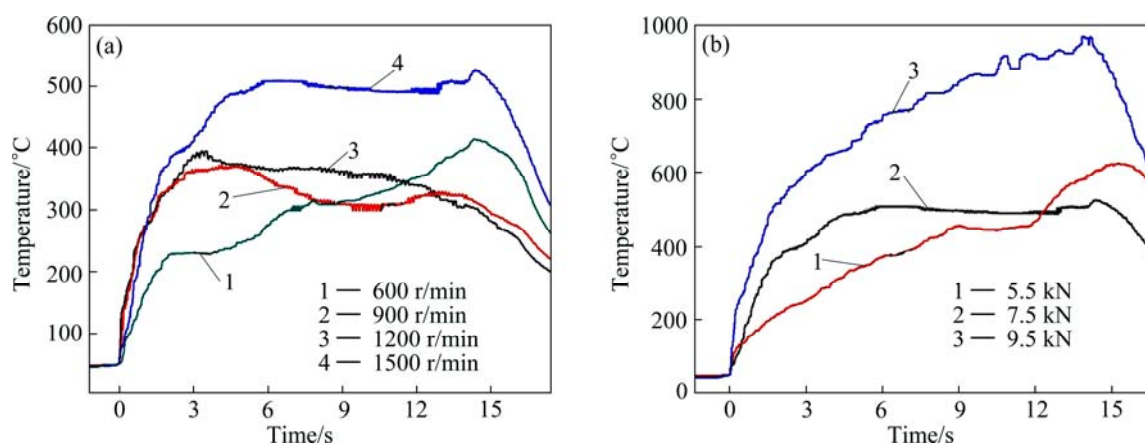

Fig. 4 Friction interface temperature—time curves: (a) Under different rotary speeds with constant axial pressure of 7.5 kN; (b) Under different axial pressures with constant rotary speed of 1500 r/min

Fig. 5 Axial displacement of carbide rod—time curves: (a) Under different rotary speeds with constant axial pressure of 7.5 kN; (b) Under different axial pressures with constant rotary speed of 1500 r/min
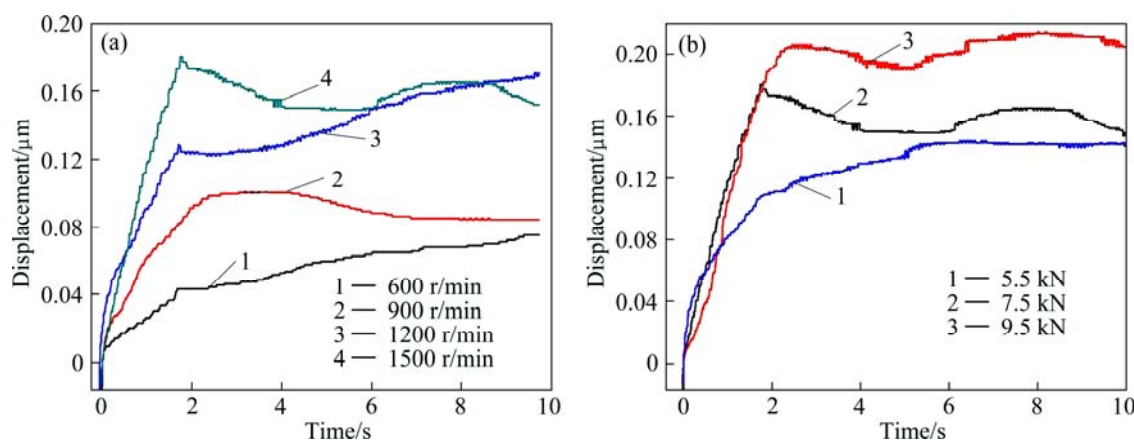
noted that the abrasion loss (w) was calculated by the following formulation:

$$w=\pi r^2 s\rho \tag{1}$$

where r is the radius of carbide rod radius, s is the final axial displacement obtained by high-speed photography, and ρ is the density of the Co based alloy. By Eq. (1), the abrasion loss at various rotary speeds and axial pressures were calculated, as shown in Fig. 6, revealing high rotary speed and high axial pressure all tend to markedly increase the abrasion loss.

3.1.4 Morphology of laser-clad coating surface after viscoplastic friction

Characteristic morphologies of the corresponding friction surfaces are revealed in Fig. 7. At a relatively low rotary speed of 600 r/min and a moderate axial
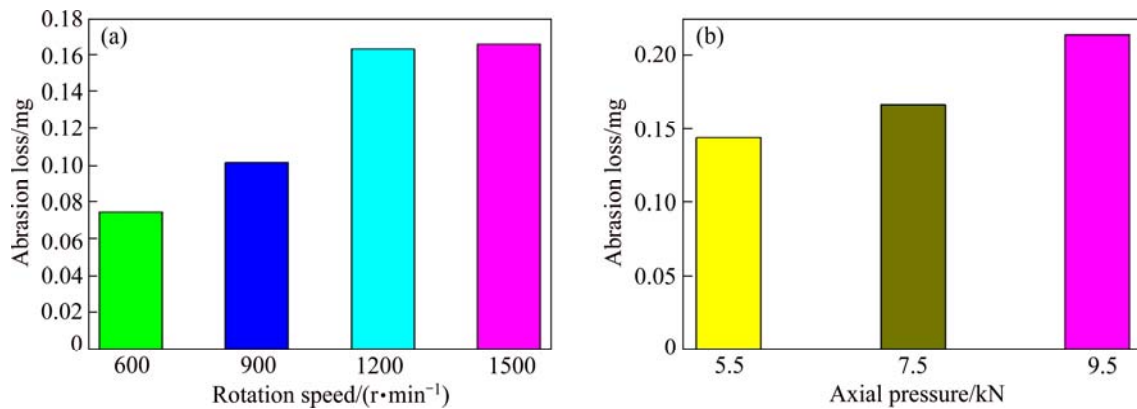

Fig. 6 Abrasion losses of laser coatings: (a) Under different rotary speeds with constant axial pressure of 7.5 kN; (b) Under different axial pressures with constant rotary speed of 1500 r/min
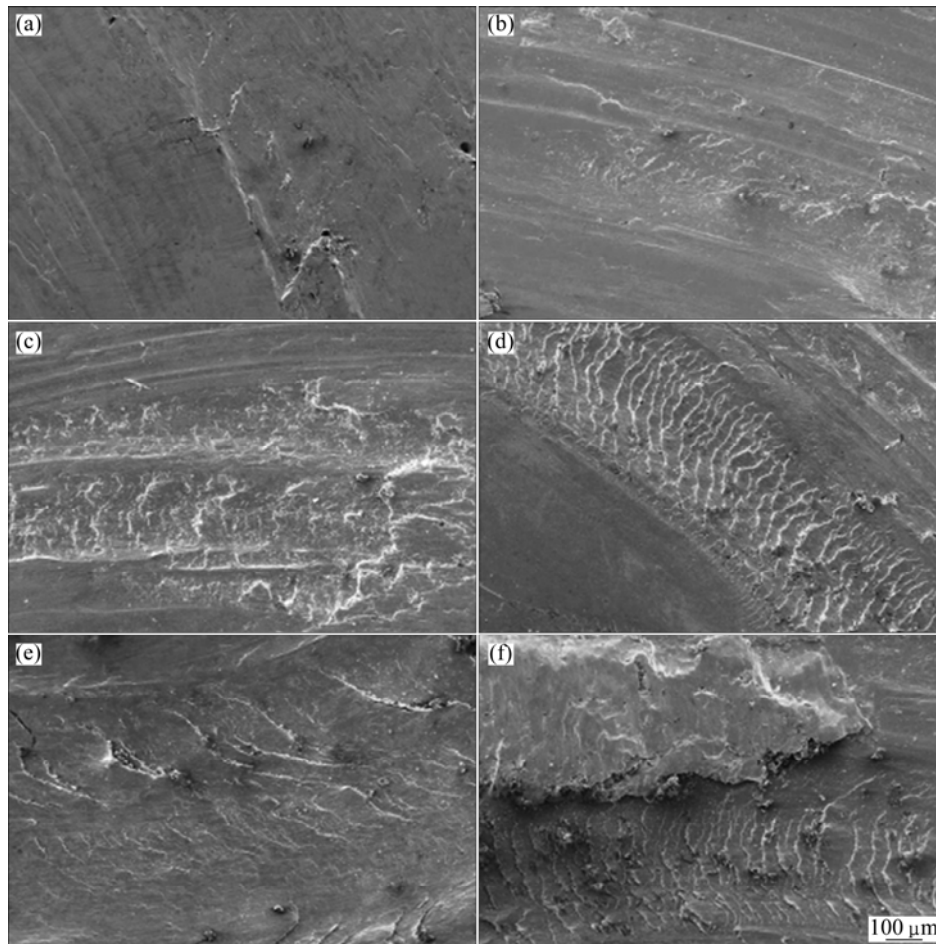

Fig. 7 SEM images of friction surfaces of laser clad coatings at different rotary speeds and axial pressures: (a) 600 r/min, 7.5 kN; (b) 900 r/min, 7.5 kN; (c) 1200 r/min, 7.5 kN; (d) 1500 r/min, 7.5 kN; (e) 1500 r/min, 5.5 kN; (f) 1500 r/min, 9.5 kN

pressure of 7.5 kN, the friction surface of laser coating primarily showed smooth grooves representing the abrasion wear (Fig. 7(a)). As rotary speed increased to 900 r/min with the fixed axial pressure of 7.5 kN, a small amount of adhesion tribolayer of viscoplastic can be observed, although the majority of the friction surface showed abrasion wear (Fig. 7(b)). When the rotary speed was further increased to 1200 r/min, the adhesion tribolayer caused by viscoplastic friction became more apparent with very little abrasion wear morphology (Fig. 7(c)). At an even higher rotary speed of 1500 r/min, the scaly plastic tribolayer was apparently and densely arranged (Fig. 7(d)). When the axial pressure was decreased to 5.5 kN with the fixed rotary speed of 1500 r/min, the trend of scaly plastic tribolayer was weakened a little (Fig. 7(e)). However, at a high axial pressure of 9.5 kN, the friction surface was all covered with scaly viscoplastic tribolayer with no abrasion wear appearance (Fig. 7(f)). Thus, it was reasonable to consider that as the high rotary speed or high axial pressure was applied, the friction mechanism changed gradually from abrasion wear to adhesion tribolayer, which was viscoplastic tribolayer in the present study.

Above all, the friction coefficient, friction interface temperature and axial displacement variations all have rising stage and steady stage, and the high rotary speed and high axial pressure can lessen the time needed to reach the steady stage. The rising stage and the steady stage are corresponding to different friction mechanisms. The rising stage belongs to sliding friction because its temperature is not high, thus the viscoplastic metal could not be formed, just yielding some wear debris. In other word, in the rising stage, the friction stress is lower than the shear yield stress of the Co based coating, thus the coating is just worn, not viscously deformed. With the accumulation of friction heat, the temperature increases rapidly, which in turn softens the Co based coating, thus the friction stress exceeds the shear stress, resulting in the viscoplastic deformation. Consequently, the rising stage belongs to sliding and the steady stage belongs to sticking [15,16]. Additionally, the high rotary speed and axial pressure could lead to more heat generation, high temperature and thereby rapid temperature rising, thus inducing the transformation from wear to viscoplastic friction.

3.2 Microstructural and hardness evolution

3.2.1 Typical microstructure induced by viscoplastic friction

The SEM images taken from the cross-section of the friction processed laser coating are shown in Fig. 8. It is obvious that after rotary friction, three typical distinct zones can be detected: 1) the top surface of viscoplastic deformation zone, which experiences the most severe plastic deformation and attendant dynamic recrystallization, forming nanograins, 2) the thermo-mechanically affected zone beneath the viscoplastic deformation zone, in which the material has been plastically deformed and the heat flux has also exerted some influence on the material without recrystallization, and 3) the original laser-clad microstructure which is not affected by the rotary friction. Figure 8(b) shows the
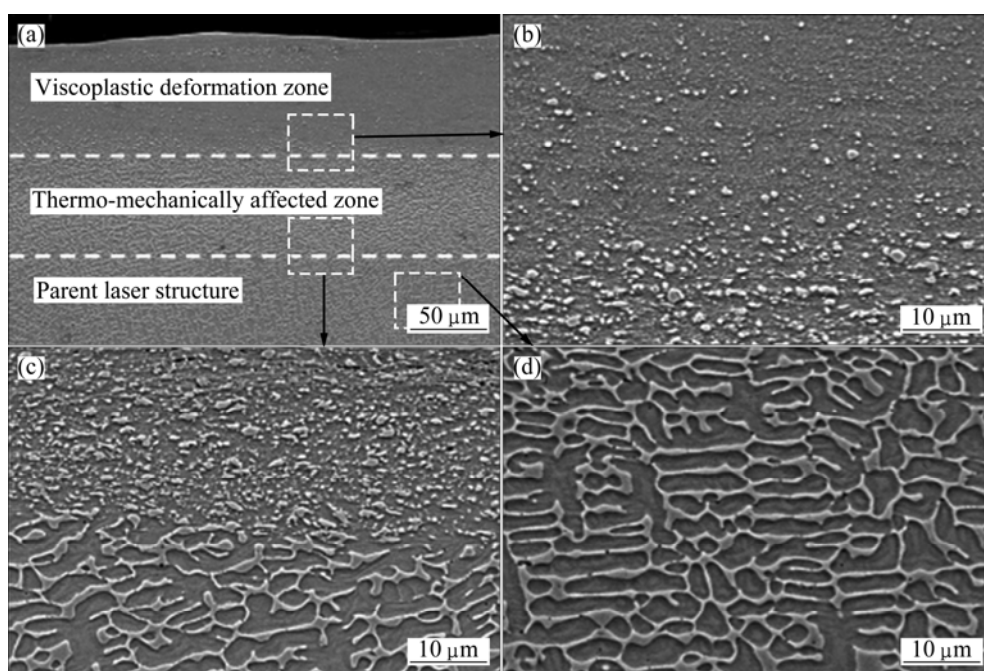

Fig. 8 SEM images of characteristic microstructures of rotation friction processed Co-based laser coating: (a) Low magnification, showing typical three zones; (b) Transition from viscoplastic deformation zone to thermal-mechanically affected zone; (c) Transition from thermal-mechanical zone to laser parent zone; (d) Characteristic laser-clad microstructure

transition zone from the viscoplastic deformation zone to thermo-mechanically affected zone. Figure 8(c) shows the transition zone from the thermo-mechanically affected zone to the original laser-clad structure. Figure 8(d) depicts the typical laser-clad microstructure, which is not affected by friction deformation, showing the mesh-distributed second phase. EDX analysis revealed that the network is $M_{23}C_6$ and the base matrix is Co-based solid solution. It is reasonable to conclude that the rotary WC−Co tool could smash the network $M_{23}C_6$ to dispersively distributed nanoparticles, meanwhile, can also considerably refine the grain of Co-based solid solution.

3.2.2 Effects of rotary conditions on viscoplastic zone thicknesses

Figure 9 illustrates clearly how the rotary speed and axial pressure affect the viscoplastic zone thicknesses. When the axial pressure was fixed as constant, generally speaking, the high rotary tended to enable a much wider viscoplastic zone, as evidenced by the metallographic picture of cross section (Fig. 9(a)). At a relatively low rotary speed of 600 r/min, the as-received viscoplastic thickness was about 37 μm. When the rotary speed increased to 900 r/min, the viscoplastic zone thickness increased to about 50 μm, which further increased to 59 μm and 58 μm, at more rapid rotary speed of 1200 r/min and 1500 r/min, respectively. Thus, it was found that with the further increase of rotary speed, the viscoplastic zone thickness reached a stable value of 50−60 μm. As the rotary speed was fixed constant (Fig. 9(b)), the viscoplastic zone thickness increased markedly with the enhancement of axial pressure. At much lower axial pressures of 5.5 kN and 7.5 kN, the viscoplastic zone thickness were 50 and 58 μm, respectively. However, when the pressure increased to 9.5 kN, the as-received viscoplastic zone thickness remarkably reached 131 μm. It is because that the high rotary speed and axial pressure could give rise to high friction stress and more heat generation and temperature field, which in turn favors the formation of plastic metal and accordingly, more wide viscoplastic zone.

3.2.3 FIB-TEM characterization of viscoplastic zone

To characterize the microstructure of viscoplastic zone, the TEM specimens were extracted from the cross sections about 10 μm below the friction surface using FIB "lift-out" technique. In order to prevent
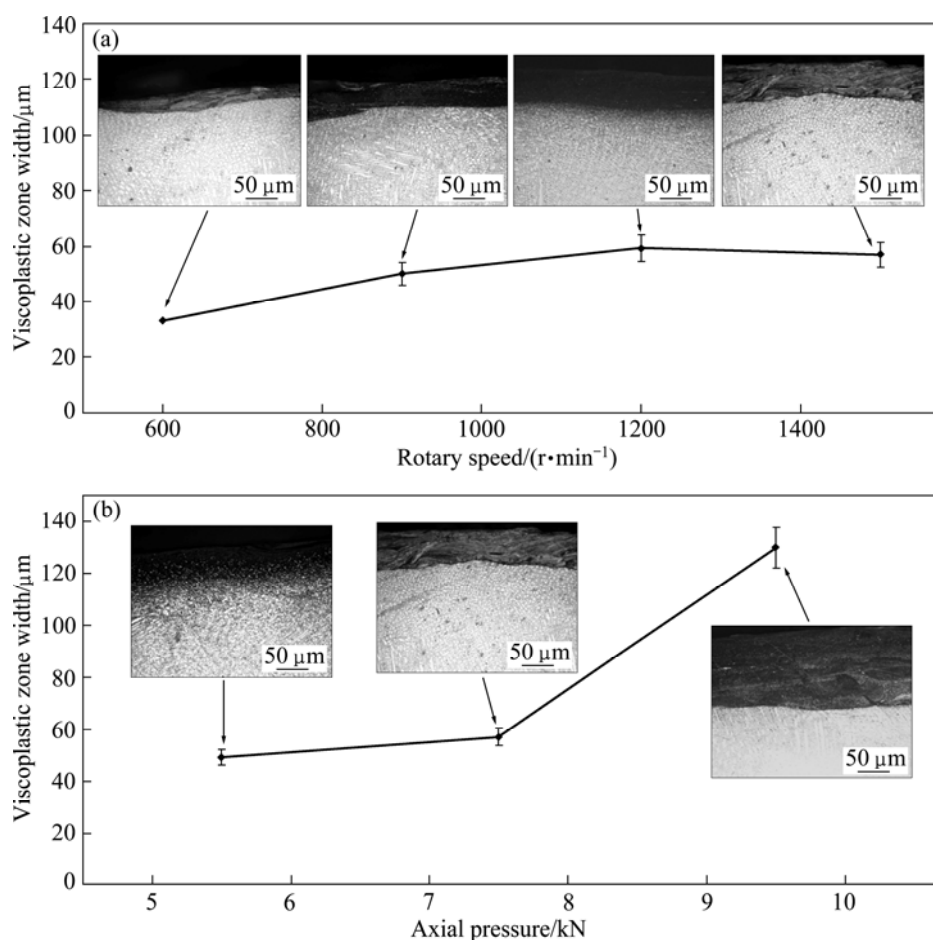

Fig. 9 Effects of friction parameters on widths of viscoplastic zones: (a) Different rotary speeds with fixed axial pressure of 7.5 kN; (b) Different axial pressures with fixed rotary speed of 1500 r/min

contamination, the TEM specimen was mounted onto the TEM Cu grid using FIB deposited tungsten prior to the final FIB thinning. Figure 10 shows the FIB "lift out" TEM sample preparation process of the viscoplastic zone. Low-magnification TEM examinations also reveal the existence of nano-scale microstructure of the viscoplastic deformation zone, as evidenced in Fig. 11(a). The circular SAED pattern also confirms the nanograins of
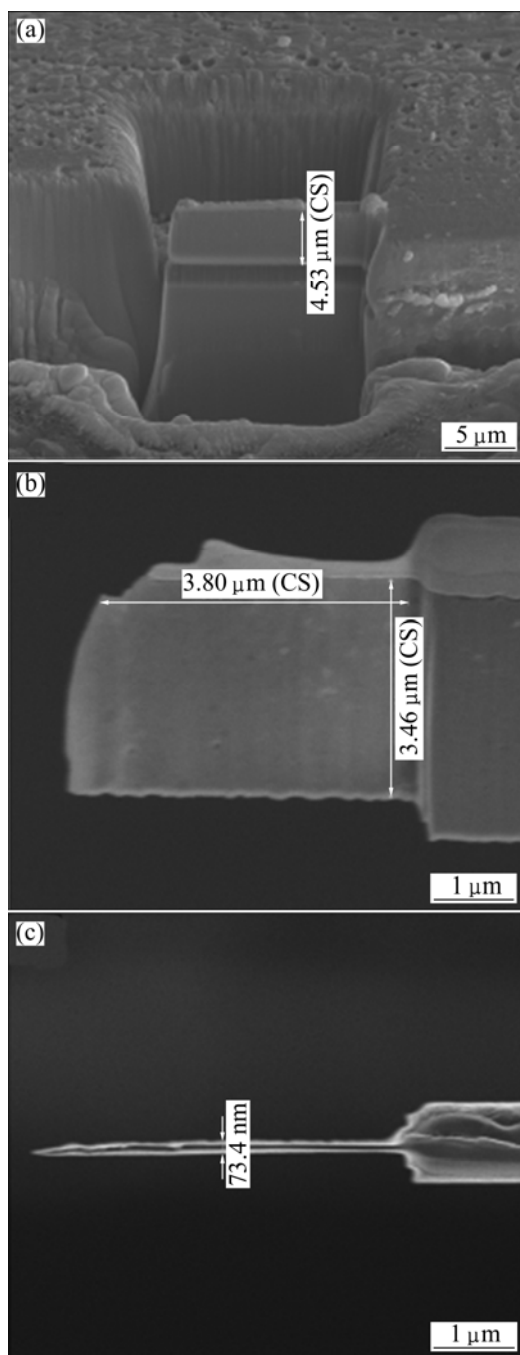
the viscoplastic deformation zone. The high-magnification TEM images (Fig. 11(b) and (c)) show the grains are bellow 50 nm with roughly equiaxed shapes, which are in agreement with the SEM results. Also, substructure and dense dislocations can be found. Figures 11(d) and (e) show the existences of α-Co-based solid solution and $(Cr,Fe,Mo)_{23}C_6$ hard phase. The $Cr_{23}C_6$ is metal rich carbide, which contains an intricate cubic structure, including 92 metal and 24 carbon atoms per unit cell, with the lattice parameter of 1.06 nm [4]. Interestingly, the near-ring shaped SAED image can be detected, as evidenced by Fig. 11(f), revealing the existence of near amorphous at the viscoplastic zone, owing to the significant refinement of grains.

HRTEM was preformed to identify the nanocrystalline phases at the viscoplastic deformation region. Figure 12(a) shows the lattice image and Figs. 12(b) and (c) are the magnified images. Figure 12(b) shows the interatomic layer distance of 4.9 Å. Combining the results of SAED pattern, one can basically determine the crystalline phase to be $M_{23}C_6$, as the lattice layer distance of the crystal examined is quite consistent with that of the $M_{23}C_6$ at the crystal face of (002). In addition, it represents that the grain size of $M_{23}C_6$ phase is about 5 nm. Figure 12(c) shows the interatomic layer distance of 1.9Å, which is compatible with that of the α-Co solid solution at the crystal face of (002). Figure 13 shows the lattice image of α-Co solid solution. It can be found that the disordered crystal surface lattice experienced severe distortion and slippage, forming many crystal defects, and accordingly the nano-scale subboundary and near amorphous, which is in accordance with the analysis of Fig. 11(f).

In general, the rotation friction, which can form the nano-scale viscoplastic zone, could be seen as SPD to refine microstructure. Considering the low stacking fault energy (SFE) of Co-based alloy, the dynamic recrystallization (DRX) is the main SPD mechanism [17]. As a result, during rotation friction, the DRX could considerably refine the microstructure and form the nanograins at the viscoplastic deformation zone. In more detail, the strain induced grain boundary migration or bulging account for the DRX grains nucleation, which occurs at the bulged boundaries of initial grains [13]. The microstructure formation is by the dynamic balance between the severe plastic strain and the restoration, in other words, the hardening and softening processes. During the rotary friction process, the high rotary speed, and resultantly, the considerably high strain rate would not leave sufficient time for the growth of dynamically formed nuclei, yielding the nanograins. Furthermore, when the plastic deformation (hardening) occurs dramatically while the softening is insufficient at some zones, the crystal lattice is broken into disordered state.
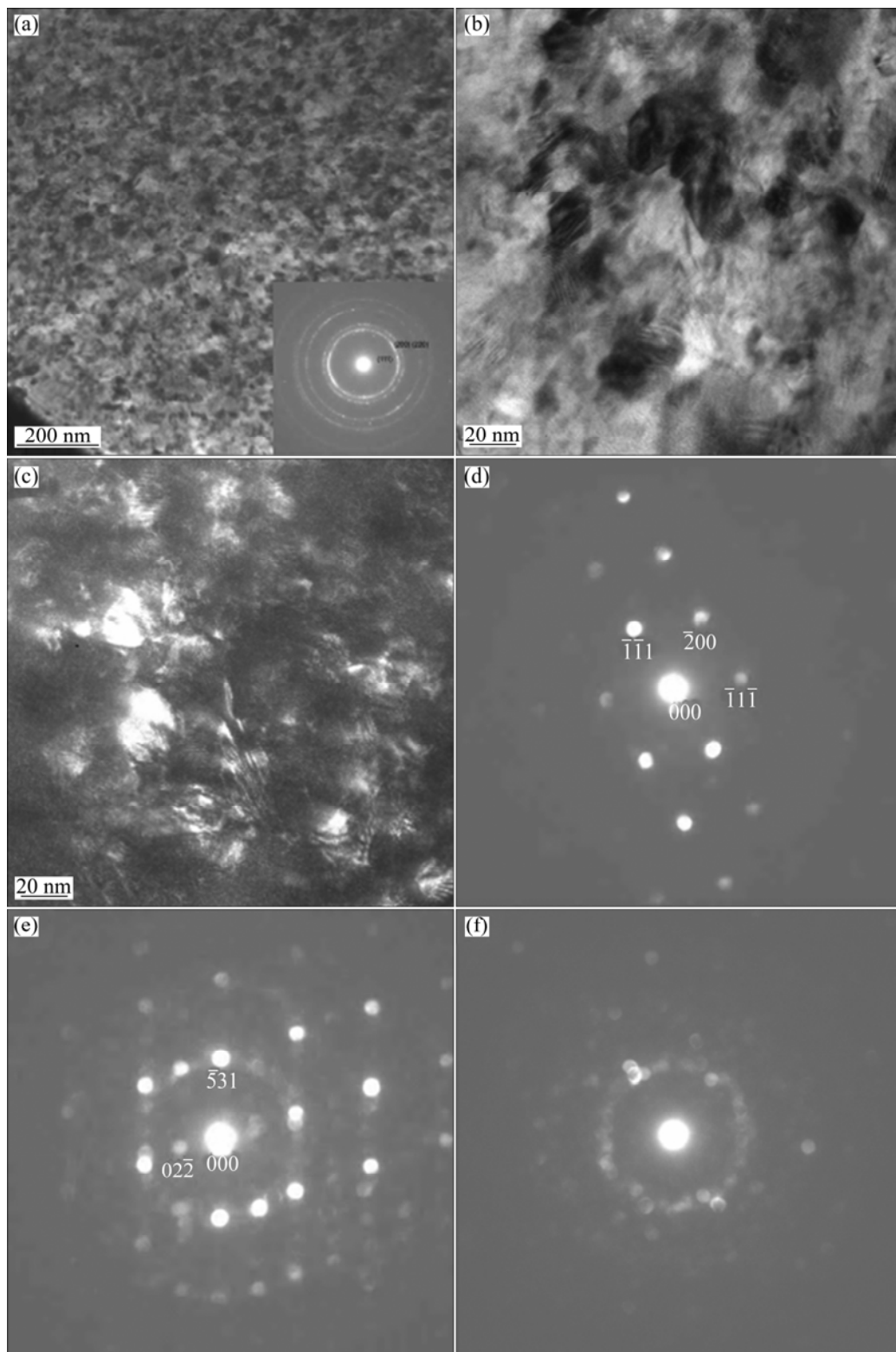

Fig. 10 FIB "lift-out" TEM specimen preparation from viscoplastic deformation zone: (a) Trenching cutting to isolate thin membrane to be lifted-out; (b) Right view FIB image of TEM foil after FIB thinning; (c) Side view FIB image of TEM foil after FIB thinning

Fig. 11 TEM images of viscoplastic zone: (a) Low-magnification bright-field image and SAED pattern; (b) High-magnification bright-field image; (c) High-magnification dark-field image; (d) SAED pattern of α-Co; (e) SAED pattern of $M_{23}C_6$; (f) SAED pattern of near amorphous

3.2.4 Microhardness of laser-clad coating after rotary friction

Figure 14 shows the microhardness depth profiles of the rotary friction processed laser-clad coating. Generally speaking, after rotary friction process the microhardness was remarkably improved from about HV 600 for the original laser structure to maximal HV 997 at the viscoplastic deformation zone. The microhardness tended
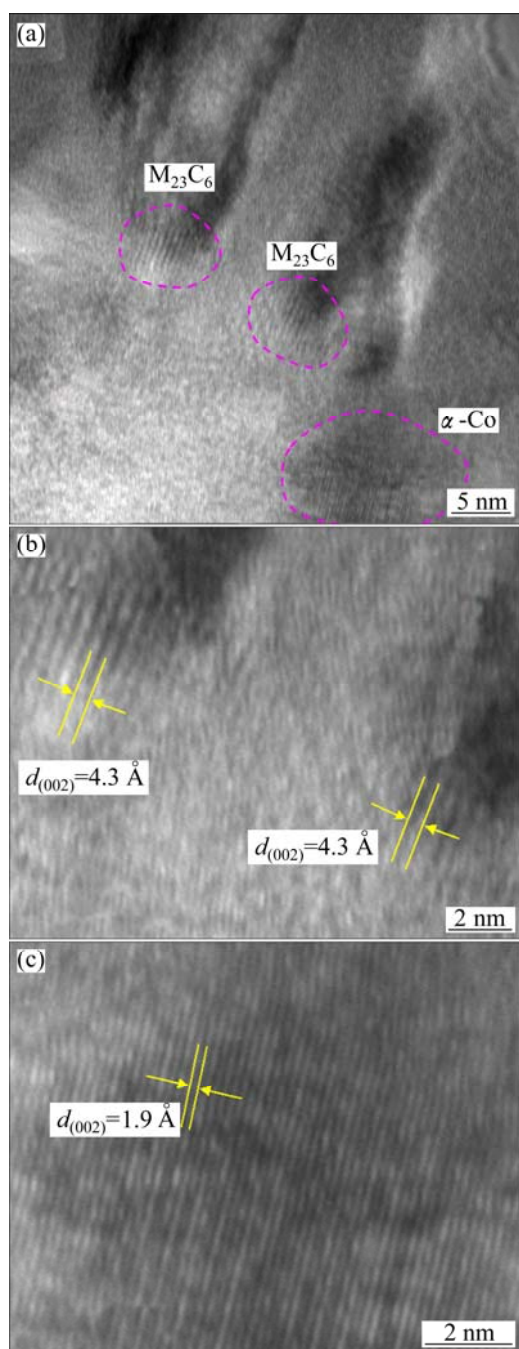
Fig. 12 HRTEM images of viscoplastic deformation zone

Fig. 13 HRTEM image of viscoplastic deformation zone showing grain boundary, subboundary and near amorphous

Fig. 14 Microhardness depth profiles of cross section of rotation friction processed laser-clad coating

4 Conclusions

1) The friction coefficient—time, friction interface temperature—time and axial displacement—time curves all experienced rising stage and then steady stage. The friction mechanism of rising stage was sliding friction while that of the steady stage was viscoplastic friction. The high rotary speed and high axial pressure could lessen the time needed to reach the steady stage, and can also increase the viscoplastic friction effect from the friction surface.

2) After viscoplastic friction, the laser-clad coating contained the three typical zones the top surface of viscoplastic deformation zone characterized by nanograins, the thermo-mechanically affected zone beneath the viscoplastic deformation zone, characterized by crushed carbide phase, and the original laser-clad microstructure characterized by the network carbide. In addition, the carbide particle size coarsened gradually from the friction surface to the parent laser zone, due to

to decrease with the increase of depth from surface, showing the reducing of microhardness from viscoplastic deformation zone, to thermo-mechanically affected zone and original laser zone. According to the well known Hall-Petch equation, the variations of hardness are inversely proportional to the grain dimension. Thereby, the smaller the grain dimension, the higher the hardness will be. Moreover, when comparing the hardness at different rotary speeds, one can notice that the high rotary speed possesses a relative high hardness. It is because that the high strain rate can induce more small-sized grains thus the high hardness.
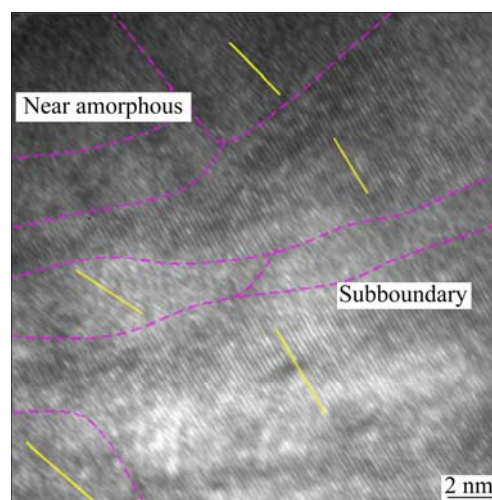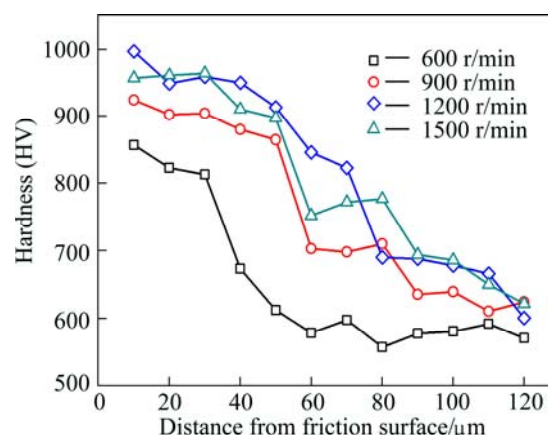
the decreased strain rate.

3) The viscoplastic zone thickness was 37−131 μm. The high rotary speed and axial pressure could give rise to high friction stress and resultantly high temperature field, which in turn favors the formation of viscoplastic metal and accordingly, more viscoplastic zone thickness.

4) FIB-TEM characterization of viscoplastic deformation zone showed that the $M_{23}C_7$ and α-Co phases were all bellow 50 nm, accompanied with a large number of lattice distortions and subboundaries. The severe viscoplastic deformation enabled the significant grain refinement even the formation of a little amount of near amorphous.

5) The nano-scale viscoplastic zone had an extremely high hardness of about HV997, which was much higher than that of the original laser coating of about HV600. Moreover, increasing the rotary speed could yield high strain rate and accordingly high hardness.

References

[1] VILAR R, SANTOS E C, FERREIRA P N, FRANCO N, DA SILVA. Structure of NiCrAlY coatings deposited on single-crystal alloy turbine blade material by laser cladding [J]. Acta Materialia, 2009, 57(18): 5292−5302.

[2] WANG S H, CHEN J Y, XUE L. A study of the abrasive wear behaviour of laser-clad tool steel coatings [J]. Surface & Coating Technology, 2006, 200(11): 3446−3458.

[3] YAN H, ZHANG P L, YU Z S, LI C G, LI R D. Development and characterization of laser surface cladding (Ti,W)C reinforced Ni−30Cu alloy composite coating on copper [J]. Optical & Laser Technology, 2012, 44(5): 1351−1358.

[4] YAN H, WANG A H, XU K D, WANG W Y, HUANG Z W. Microstructure and interfacial evaluation of Co-based alloy coating on copper by pulsed Nd:YAG multilayer laser cladding [J]. Journal of Alloy and Compounds, 2010, 505(2−3): 645−653.

[5] GU D D, HAGEDOMRN Y C, MEINERS W, MENG G B, BATISTA R J S, WISSENBACH K, POPRAWE R. Densification behavior, microstructure evolution, and wear performance of selective laser melting processed commercially pure titanium [J]. Acta Materialia, 2012, 60(9): 3849−3860.

[6] GU D D, MENG G B, LI C, MEINERS W, POPRAWE R. Selective laser melting of TiC/Ti bulk nanocomposites: Influence of nanoscale reinforcement [J]. Scripta Materialia, 2012, 67(2): 185−188.

[7] GU D D, HONG C, MENG G B. Densification, microstructure, and wear property of in situ titanium nitride-reinforced titanium silicide matrix composites prepared by a novel selective laser melting process [J]. Metallurgical and Materials Transactions A, 2012, 43(2): 697−708.

[8] MISHRA R S, MA Z Y. Friction stir welding and processing [J]. Materials Science and Engineering R, 2005, 50(1−2): 1−78.

[9] SIRCAR S, SINGH J, MAZUMDER J. Microstructure evolution and nonequilibrium phase-diagram for Ni−Hf binary alloy produced by laser cladding [J]. Acta Metall Mater, 1989, 37(4): 1167−1176.

[10] HE T T, XIONG Y, REN F Z, GUO Z Q, VOLINSKY A A. Microstructure of ultra-fine-grained high carbon steel prepared by equal channel angular pressing [J]. Materials Science and Engineering A, 2012, 535(15): 306−310.

[11] YODA R, SHIBATA K, MORIMITSU T, TERADA D, TSUJI N. Formability of ultrafine-grained interstitial-free steel fabricated by accumulative roll-bonding and subsequent annealing [J]. Scripta Materialia, 2011, 65(3): 175−178.

[12] CHANG C I, DU X H, HUANG J C. Producing nanograined microstructure in Mg−Al−Zn alloy by two-step friction stir processing [J]. Scripta Materialia, 2008, 59(3): 356−359.

[13] MEHRANFAR M, DEHGHANI K. Producing nanostructured super-austenitic steels by friction stir processing [J]. Materials Science and Engineering A, 2011, 528(9): 3404−3408.

[14] LI R D, SHI Y S, WANG Z G, WANG L, LIU JH, JIANG W. Densification behavior of gas and water atomized 316L stainless steel powder during selective laser melting [J]. Applied Surface Science, 2010, 256(13−15): 4350−4356.

[15] MAALEKIAN M, KOZESCHNIK E, BRANTNER H P, CERIAK H. Comparative analysis of heat generation in friction welding of steel bars [J]. Acta Materialia, 2008, 56(12): 2843−2855.

[16] LI R D, LI J L, XIONG J T, ZHANG F, S, ZHAO K, JI C Z. Friction heat production and atom diffusion behaviors during Mg−Ti rotating friction welding process [J]. Transactions of Nonferrous Metals Society of China, 2012, 22(11): 2665−2671.

[17] CHIBA A, LEE S H, MATSUMOTO H, NAKAMURA M. Construction of processing map for biomedical Co−28Cr−6Mo−0.16N alloy by studying its hot deformation behavior using compression tests [J]. Materials Science and Engineering A, 2009, 513−514(15): 286−293.

激光熔覆 Co−Cr−Ni−Mo 涂层的粘塑性摩擦及组织演变行为

李瑞迪[1,2]，李京龙[1,2]，梁　毅[1,2]，籍成宗[1,2]，袁铁锤[3]

1. 西北工业大学 凝固技术国家重点实验室，西安　710072；

2. 西北工业大学 陕西省摩擦焊接重点实验室，西安　710072；3. 中南大学 粉末冶金国家重点实验室，长沙　410083

摘　要：通过激光熔覆 Co−Cr−Ni−Mo 合金与 WC−Co 硬质合金之间的旋转摩擦变形实验，研究钴基合金的粘塑性摩擦及纳米组织形成机制。考察粘塑性摩擦过程的摩擦系数、界面温度及轴向缩短量随时间的变化关系。结果表明以上物理量首先进入快速上升阶段，然后进入稳态阶段，其中第一个阶段属于滑动摩擦，第二阶段属于粘塑性摩擦。粘塑性摩擦后，激光熔覆涂层从表面至内部可分为粘塑性变形区、热力影响区、激光原始组织 3 个典型区域。粘塑性变形可将原始组织中的网状 $M_{23}C_7$ 相破碎为弥散分布的等轴形状纳米晶粒。粘塑性区的宽度为 37~131 μm，其典型组织特征为晶粒尺度小于 50 nm 的 $M_{23}C_7$ 相及 α-Co 相，甚至含有少量接近非晶态结构。因而，粘塑性摩擦将激光熔覆合金的硬度由 HV600 提高至 HV997。

关键词：粘塑性摩擦；剧烈塑性变形；激光熔覆；Co−Cr−Ni−Mo 涂层；纳米结构；旋转摩擦

(Edited by Sai-qian YUAN)